Contents lists available at ScienceDirect

Electrochimica Acta

The development of a fully integrated 3D printed electrochemical platform and its application to investigate the chemical reaction between carbon dioxide and hydrazine

João Giorgini Escobar [a], Eva Vaněčková [b,c], Štěpánka Nováková Lachmanová [b], Federico Vivaldi [d], Jan Heyda [c], Jiří Kubišta [b], Violetta Shestivska [b], Patrik Španěl [b], Karolina Schwarzová-Pecková [e], Jiří Rathouský [b], Táňa Sebechlebská [b,f,**], Viliam Kolivoška [b,*]

[a] Institute of Chemistry, UNB - University of Brazilia, Campus Universitário Darcy Ribeiro 70910-900 Asa Norte - Brasília-DF, Brazil
[b] J. Heyrovský Institute of Physical Chemistry of the Czech Academy of Sciences, Dolejškova 3, 18223 Prague, Czechia
[c] Department of Physical Chemistry, Faculty of Chemical Engineering, University of Chemistry and Technology Prague, Technická 5, 166 28 Prague 6, Czechia
[d] Department of Chemistry and Industrial Chemistry, University of Pisa, Via Giuseppe Moruzzi 13, 56124 Pisa, Italy
[e] UNESCO Laboratory of Environmental Electrochemistry, Department of Analytical Chemistry, Faculty of Science, Charles University, Hlavova 8, 128 43 Prague, Czechia
[f] Department of Physical and Theoretical Chemistry, Faculty of Natural Sciences, Comenius University in Bratislava, Mlynská Dolina, Ilkovičova 6, 84215 Bratislava 4, Slovakia

ARTICLE INFO

ABSTRACT

The combination of computer assisted design and 3D printing has recently enabled fast and inexpensive manufacture of customized 'reactionware' for broad range of electrochemical applications. In this work bi-material fused deposition modeling 3D printing is utilized to construct an integrated platform based on a polyamide electrochemical cell and electrodes manufactured from a polylactic acid-carbon nanotube conductive composite. The cell contains separated compartments for the reference and counter electrode and enables reactants to be introduced and inspected under oxygen-free conditions. The developed platform was employed in a study investigating the electrochemical oxidation of aqueous hydrazine coupled to its bulk reaction with carbon dioxide. The analysis of cyclic voltammograms obtained in reaction mixtures with systematically varied composition confirmed that the reaction between hydrazine and carbon dioxide follows 1/1 stoichiometry and the corresponding equilibrium constant amounts to $(2.8 \pm 0.6) \times 10^3$. Experimental characteristics were verified by results of numerical simulations based on the finite-element-method.

© 2020 Elsevier Ltd. All rights reserved.

1. Introduction

The recent decade has witnessed an expansion of 3D printing (3DP) technologies into each and every field of science involving electrochemistry [1,2]. Approaches of 3DP create objects by posi-

tioning target material on previously formed layers. The combination of 3DP with computer assisted design (CAD) allows rapid, inexpensive, safe and environmentally friendly manufacture of customized 'reactionware' (cells and electrodes) directly in an electrochemical laboratory.

Electrochemical cells manufactured by 3DP offer several advantages over their glass counterparts: (I) cells may be printed directly in a chemical laboratory without specially trained personal, (II) CAD allows rapid prototyping and redesign of cells, (III) cells with complicated inner structure may be created, (IV) 3DP cells are significantly less breakable than glass cells, (V) 3DP offers considerable reduction of material and energy consumption. The first 3DP electrochemical cell was constructed by Symes et al. [3] in 2012 by extruding acetoxysilicone polymer through a syringe and casting it onto a glass substrate. Presently, the most widely used 3DP technologies are selective laser melting (SLM), stereolithography

* Corresponding author.
** Corresponding author.
   E-mail addresses: joaogiorgini@gmail.com (J. Giorgini Escobar), eva.vaneckova@jh-inst.cas.cz, vaneckoe@vscht.cz (E. Vaněčková), stepanka.lachmanova@jh-inst.cas.cz (Š. Nováková Lachmanová), federico-vivaldi@virgilio.it (F. Vivaldi), Jan.Heyda@vscht.cz (J. Heyda), jiri.kubista@jh-inst.cas.cz (J. Kubišta), violetta.shestivska@jh-inst.cas.cz (V. Shestivska), patrik.spanel@jh-inst.cas.cz (P. Španěl), karolina.schwarzova@natur.cuni.cz (K. Schwarzová-Pecková), jiri.rathousky@jh-inst.cas.cz (J. Rathouský), tana.sebechlebska@jh-inst.cas.cz, tana.sebechlebska@uniba.sk (T. Sebechlebská), viliam.kolivoska@jh-inst.cas.cz (V. Kolivoška).

Table 1
Summary of works emploIying cells manufactured by fused deposition modelling 3D printing.

Material	Cell functionality	Working electrode	Application	Ref.
PLA	liquid/gas cells with a 3D printed separator	stainless steel (SLM technique)	water electrolysis	[7]
	simple cell, no functionality	stainless steel (SLM technique)	water electrolysis	[8]
	flow cell	PLA/graphene	determination of catechol	[14]
	flow cell with a gas purging system	fluorine-doped tin oxide on glass	wastewater cleaning	[15]
	flow cell	iron	electrosynthesis of magnetite particles	[16]
	simple cell, no functionality	PLA/carbon black	determination of Hg^{2+} ions	[17]
	simple cell, no functionality	PLA/carbon black	determination of Hg^{2+} ions, caffeine and H_2O_2	[18]
	two compartment cell with gas purging system, devided by a membrane	Pd nanocubes-modified glassy carbon	electrooxidation of glycerol	[19]
ABS	flow capillary cell	Prussian blue/ gold	determinantion of H_2O_2	[20]
	flow cell for batch injection analysis	PLA/graphene	determination of tert-butylhydroquinone, dipyrone, dopamine and diclofenac	[21]
	flow cell separated by a membrane	nickel foil	mass transport characterization	[22]
	cell for batch injection analysis	Prussian blue/carbon	determination of glucose	[23]
	spectroelectrochemical cell	PLA/graphene	Raman spectroelectrochemistry	[24]
	flow cell	copper	characterization of current distribution	[25]
	Y-shaped flow cell	pencil (graphite)	enzymatic glucose biofuel cell	[26]
	simple cell, no functionality	PLA/carbon black	determination of organic acids and dopamine	[27]
	two compartment cell connected by a salt bridge	PLA/graphene, PLA/carbon black	water electrolysis	[28]
	Y-shaped flow cell	reduced graphene oxide	determination of dopamine	[29]
polypropylene	flow cell separated by a membrane	silver	water electrolysis	[30]
	packed-bed scalable electrochemical reactor	boron-doped diamond	electrosynthesis of graphene oxide	[31]
	flow cell	carbon	methoxymethylation of alcohols	[32]
co-polyester	electrochemical biosensor	screen-printed gold electrodes modified by antibodies	determination of tumor cells	[33]
polyamide 12	three compartment cell connected by Luggin capillaries, dedicated to liquid/liquid electrochemistry	platinum	determination of ephedrine	[34]

(SLA) and fused deposition modelling (FDM) [4]. The SLM technique creates objects by fusing atomized metallic powders melted locally by a laser beam and was applied to manufacture metallic electrodes for supercapacitors [5] and water electrolysers [6–8]. Recently, multi-material mode of SLM technique employing stainless steel, titanium and graphite was utilized to manufacture integrated proton exchange membrane electrolyzer cells [9]. The SLA technique forms objects from layers of resins polymerized locally by a laser-induced photochemical process. This technique was employed to develop cells for water electrolysis [10], spectroelectrochemical measurements [11] and electroanalytical applications [12]. Though the first conductive resins have been recently synthesized [13], values of their electric conductivity are insufficient to manufacture electrodes. The FDM as the most common and versatile 3DP technique relies on extruding filament through a heated nozzle. Low expenses and wide availability of printers render the FDM particularly suitable for the manufacture of cells. Most frequently used filaments are polylactic acid (PLA), [8,7,14–19] acrylonitrile butadiene styrene (ABS), [20–29] polypropylene [30–32], and polyesters [33]. Cells manufactured by FDM 3DP involve multitude of functionalities and have found use in a broad range of electrochemical processes and applications, which are summarized in Table 1. However, none of these cells allows a fundamental analysis of electron transfer processes and related phenomena which requires strictly oxygen-free environment, separated compartments for working, counter and reference electrode and an interface to introduce reaction components. The goal of this work is the development, manufacture and inspection of such cell design.

Recent advancements in the preparation of printable conductive composite materials enabled the use of FDM to manufacture electrodes. In the pioneering work of Rymansaib et al. [35] polystyrene was blended with graphite and carbon nanofibers to extrude a conductive composite filament further employed to print electrodes for the electroanalytical determination of Pb^{2+} ions. Following works employed commercial composites of PLA with graphene, [14,21,24,28,36,37] carbon black [17,18,28,38–40], carbon nan-

otubes [41] and copper [42] as conductive fillers. Electrodes manufactured from in-lab synthesized PLA-based composites containing $MoSe_2$, carbon/platinum [43] and graphite [44] used as conductive additives were reported recently. Furthermore, commercial carbon-loaded ABS filaments were employed [17,45]. Bi-material FDM 3D printing combining conductive composites for electrodes and insulating filaments for cells enabled the manufacture of integrated platforms dedicated to electroanalysis [14,17,18,21,27,35,45] and Raman spectroelectrochemistry [24].

In this work we employ CAD combined with bi-material FDM 3DP to devise and manufacture a fully integrated electrochemical platform based on a three-compartment polyamide (PA12) cell and a PLA-carbon nanotube (PLA-CNT) composite working electrode. Employing cyclic voltammetry with the reversible electroactive probe we have recently demonstrated that PLA-CNT electrodes activated by an anodic oxidation exhibit area of the electrochemically active surface very close to the geometrical surface area. The ratio of the two quantities, further reffered to as relative area of the electrochemically active electrode surface, is thus close to unity. Cyclic voltammetric experiments with the electroactive probe further revealed that activated PLA-CNT electrodes show interfacial electron transfer rate very similar to conventionally used metallic or carbon electrodes [41]. Electrodes prepared by the reported manufacture/activation protocol are integrated with the 3DP electrochemical cell developed in this work. Importantly, the presented design allows reactants to be introduced and investigated in the oxygen free environment. The platform is designed for a systematic analysis of electron transfer processes coupled with bulk chemical reactions, which is not yet reported in the literature.

It is generally accepted that global warming is caused by rising levels of carbon dioxide largely generated by anthropogenic sources [46]. One of the strategies to mitigate the impact of human activities on the environment is the capture of carbon dioxide and its subsequent conversion to added-value chemicals [47,48]. Aqueous solutions of amines are seen as promising agents for the CO_2 capture [49–52] Hydrazine, as the smallest diamine, poten-

tially offers higher absorption capacity compared to organic amines and is thus considered as a particularly attractive CO_2 sorbent [53,54]. Furthermore, hydrazine was utilized to eliminate other environmental pollutants including halogens [55], heavy metal ions [56,57], or NO_x [58,59]. Importantly, hydrazine may be generated electrochemically [60] and if renewable energy sources are utilized in this process, it is produced without generating carbon dioxide. Motivated by the environmental potential of hydrazine we apply the electrochemical platform developed in this work to investigate the electrochemical oxidation of aqueous hydrazine coupled to its bulk reaction with carbon dioxide. We utilize cyclic voltammetry to determine the equilibrium concentration of hydrazine in its reaction mixtures with carbon dioxide and employ obtained results to determine the equilibrium constant of the reaction considering several possible stoichiometric scenarios. Experimentally obtained characteristics are corroborated by the results of finite-element-method numerical simulations.

2. Experimental section

2.1. Materials and chemicals

In all experiments performed in this work MilliQ deionized water (Millipore, France, maximum total organic carbon 3 ppb, minimum electric resistivity 18.2 MΩ cm) was used. All glassware (U-cell for the electrochemical activation of electrodes, volumetric flasks and beakers) and PTFE parts (magnetic stirrer) were cleaned by boiling in diluted (25 %) nitric acid (Lach-Ner, Czech Republic). Upon cooling down the glassware to the ambient temperature it was boiled in water four times and dried overnight at 105 °C. This purification protocol is known to guarantee cleanliness required to successfully perform sensitive electrochemical experiments that include desorption of self-assembled monolayers at monocrystalline surfaces [61] or charge transport studies performed at a single molecule level [62]. Ruthenium acetylacetonate (97 %, further abbreviated as $Ru(acac)_3$) was obtained from Sigma-Aldrich. Sodium sulfate (99.99 %, Suprapure, anhydrous) was obtained from Merck. Potassium sulfate (p.a.) was purchased from Lach-ner. Hydrazine (reagent grade, 50 – 60 % aqueous solution) was obtained from Sigma-Aldrich. Compressed gaseous argon (200 bar, 99.996 %) was purchased from Messer. Solid CO_2 (dry ice) was obtained from Linde. Natural polyamide 12 (PA12) filament was purchased from Devil Design, Poland. Electrically conductive polylactic acid-carbon nanotube (PLA-CNT) composite filament (brand name Alfaohm) was obtained from Filoalfa, Italy. Both PA12 and PLA-CNT filaments have the diameter of 1.75 mm. All 3D printed objects used in this work (the electrochemical cell including the lid, electrodes) were manufactured by FDM 3DP employing Prusa I3 MK3S 3D printer, E3D V6 brass nozzle (diameter 0.40 mm) and smooth spring steel sheet printing surface coated with polyetherimide (all three items purchased from Prusa Research, Prague, Czech Republic).

2.2. Cell design and manufacture

The electrochemical cell is dedicated to experiments in a three-electrode arrangement – involving working (WE), reference (RE) and counter (CE) electrode. The cell was devised by computer assisted design (CAD) employing the environment of Autodesk Fusion 360 (Autodesk Inc., USA). CAD drawing of the cell and its cross section is visualized in Fig. 1A and 1B, while a photograph of the cell under operating conditions is displayed in Fig. 1C. Further details on the cell design, manufacture and inspection are in the Supplementary Information.
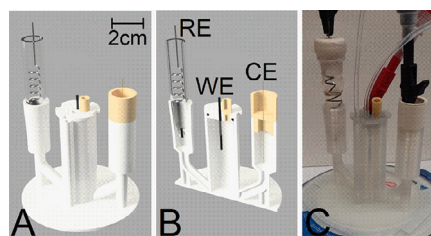

Fig. 1. (A) Full and (B) cross-sectional CAD drawing of the integrated electrochemical platform devised, manufactured and inspected in this work. (C) Photograph of the platform under operating conditions.

2.3. Electrode design, manufacture, activation and inspection of interfacial electron transfer properties

Working electrodes have cylindrical shape (diameter 1.75 mm, height 40 mm) and were printed employing a 0.40 mm nozzle with layer height set to 0.05 mm. All other printing parameters were identical to those reported previously [41]. Just before the experiment the WE was activated by anodic polarization in aqueous 0.3 M Na_2SO_4 at +6.0 V for 10 s (for details see Ref. [41]). Upon the activation, the WE was briefly rinsed in water, dried in the air and masked by a PTFE tape leaving a part with height of 12 mm exposed (geometrical electrode/electrolyte interface area 0.84 cm^2 obtained by calculations employing CAD, procedure not shown). The performance of manufactured electrodes was inspected by measuring their electron transfer properties by cyclic voltammetry performed in deaerated aqueous 0.1 M K_2SO_4 supporting electrolyte containing 5×10^{-4} M $Ru(acac)_3$ electroactive probe in the PA12 cell designed and manufactured as discussed in the Supplementary Information. For details on the cell assembly and operation, see Electrochemical measurements part that follows. The Faradaic peak-to-peak separation and the relative area of the electrochemically active electrode surface were evaluated as discussed in Ref. [41].

2.4. Electrochemical measurements

All electrochemical measurements were carried out in the PA12 cell designed and manufactured as discussed in the Supplementary Information. The WE compartment of the cell was filled with 0.1 M K_2SO_4 supporting electrolyte containing 3.85×10^{-3} M NH_2NH_2. The RE and CE compartments were filled by applying a vacuum generated by a syringe/piston/needle assembly operating through a rubber septum. Subsequently, RE and CE were introduced. The solution left in the WE compartment was discarded and a fresh solution with volume of 17.0 mL (denoted as V_{NH2NH2} in the Results and Discussion section) was added. A magnetic stirrer was introduced. The lid equipped with freshly activated WE was inserted, closing the cell. The cell assembly was finalized by connecting electrodes to the potentiostat (PGSTAT Autolab, Metrohm, Czech Republic), attaching the inlet/outlet tubing system (Fig. 1C) and purging the WE compartment by a gentle stream of argon gas saturated with the identical aqueous hydrazine solution for 5 minutes. Electrochemical measurements were performed in the staircase cyclic voltammetry regime at electrode polarization rate of 25 mV s^{-1} and potential step of 1 mV. Before each measurement, electrochemical impedance spectroscopic measurement was performed in the double-layer capacitance region of the inspected system at 5 mV AC peak-to-peak amplitude and AC frequency ranging from 10^5 to 10^0 Hz. The value of the electric resistance was extracted graphically from the real part of the impedance in the Nyquist plot (data not shown). Such obtained value multiplied by a factor of 90 – 95 % was employed as the input parameter for
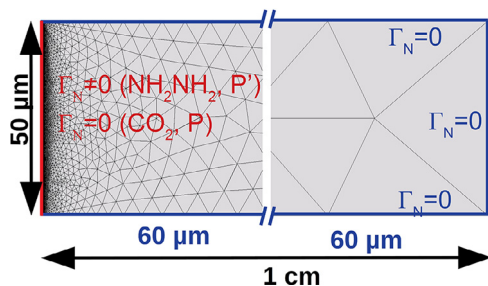
Fig. 2. Schematic depiction of the computational domain. Γ_N denotes the Neumann boundary condition at the electrode (red) and insulating walls (blue). (For interpretation of the references to color in this figure legend, the reader is referred to the web version of this article.)

positive feedback electronics to compensate voltage losses between the WE and the RE.

The cyclic voltammetry was first carried out in the absence of CO_2. Subsequently, desired amount of CO_2 was introduced as follows. Saturated aqueous solution of CO_2 was prepared by bubbling sublimated dry ice through water for at least one hour while continuously monitoring the gas pressure and the solution temperature. The concentration of CO_2 in its saturated solution (denoted as $c_{0, CO2}$) was calculated employing Henry's law and solubility-temperature profiles reported for CO_2 at standard pressure [63]. The pressure of 1.01 bar and temperature ranging from 294 to 297 K were applied. Obtained values of $c_{0, CO2}$ range from 4.05 to 3.68 $\times 10^{-2}$ M. The saturated solution of CO_2 was introduced to the WE compartment of the cell by an air-tight syringe/piston/needle assembly through the septum in the lid. The volume of the solution V_{CO2} ranged from 0.5 to 2.0 mL. The resulting NH_2NH_2/CO_2 reaction mixture was homogenized by a magnetic stirrer at 500 rpm for 5 minutes. The concentration of unreacted NH_2NH_2 was determined by cyclic voltammetry (see Results and Discussion section for details). In a control experiment, the entire procedure was precisely repeated with saturated solution of Ar instead of CO_2.

3. Calculation section

3.1. Finite-element-method numerical simulations

The interfacial electron transfer process (irreversible oxidation of hydrazine involving four electrons) and the bulk chemical reaction (synthesis of NH_2NH_2 and CO_2) studied experimentally in this work were further modelled theoretically in COMSOL Multiphysics 5.2a software [64]. The reaction scheme is summarized in Fig. 6. The electrolyte phase is represented by a 2D computational domain of a rectangular shape with length of 1×10^{-2} m and height of 5×10^{-5} m (Fig. 2). In the domain, governing continuity equations were formulated for concentration values of considered system constituents – NH_2NH_2, CO_2, the product of their bulk synthetic reaction $NH_2NH_2CO_2$ (denoted as P, assuming 1/1 reaction stoichiometry, see Results and Discussion for details) and products of the hydrazine oxidation $N_2 + 4H^+$ (cumulatively denoted as P´). The computational domain was divided to triangular non-uniform mesh with the highest density of points near the electrode (Fig. 2, left, shown in red). The electrode boundary involved 500 points. The maximum element size was set to 5×10^{-5} m, the minimum element size to 3×10^{-5} m, the maximum element growth rate to 1.2 and the curvature factor to 0.3.

3.2. The kinetic model

It formulates the bulk reaction between NH_2NH_2 and CO_2 employing reaction rate (source/sink) terms in continuity equations.

Table 2
Physical constants and parameters used in numerical simulations.

Constant/parameter and its symbol	Value and unit
standard redox potential E^0	0.7 V
number of transferred electrons n	4
standard heterogeneous rate constant k^0	1×10^{-2} m s^{-1} [a]
electrode polarization rate v	± 0.025 V.s^{-1}
electron transfer coefficient α	0.5
diffusion coefficient D_{CO2}	1.97×10^{-9} m^2 s^{-1} [b]
diffusion coefficient D_P	1.97×10^{-9} m^2 s^{-1}
diffusion coefficient D_{NH2NH2}	2.37×10^{-9} m^2 s^{-1} [c]
diffusion coefficient $D_{P'}$	2.37×10^{-9} m^2 s^{-1}
equilibrium constant K	2800 [d]
forward homogeneous rate constant k_f^{bulk}	1, 5, 7 and 10×10^9 M^{-1} s^{-1}
ideal gas constant R	8.314 J mol^{-1} K^{-1}
Faraday constant F	9.6485×10^4 C mol^{-1}
absolute temperature T	298 K

[a] taken from Ref. [67]
[b] taken from Ref. [66]
[c] taken from Ref. [65]
[d] obtained experimentally in this study.

Altogether four continuity equations are formulated and solved for individual system constituents

$$\partial[NH_2NH_2]/\partial t + \nabla.(-D_{NH2NH2}\nabla[NH_2NH_2]) + k_f^{bulk}[NH_2NH_2][CO_2] = k_b^{bulk}[P] \tag{1}$$

$$\partial[CO_2]/\partial t + \nabla.(-D_{CO2}\nabla[CO_2]) + k_f^{bulk}[NH_2NH_2][CO_2] = k_b^{bulk}[P] \tag{2}$$

$$\partial[P]/\partial t + \nabla.(-D_P\nabla[P]) + k_b^{bulk}[P] = k_f^{bulk}[NH_2NH_2][CO_2] \tag{3}$$

$$\partial[P']/\partial t + \nabla.(-D_{P'}\nabla[P']) = 0 \tag{4}$$

Values of k_f^{bulk} and k_b^{bulk} were calculated as delineated in the Results and Discussion section Eqs. (20) and ((21)). The D_{NH2NH2} value of 2.37×10^{-5} cm^2 s^{-1} was taken from Ref. [65] and the same value was assumed for $D_{P'}$. The D_{CO2} value of 1.97×10^{-5} cm^2 s^{-1} was taken from Ref. [66] and the same value was used for D_P. Employing Stokes-Einstein equation and related concepts one can easily demonstrate that these two assumptions generate the relative error in the theoretically obtained Faradaic current of less than 10 %. Values of D and all other constants and parameters employed in numerical simulations are summarized in Table 2.

3.3. The thermodynamic model

It postulates that the bulk reaction between NH_2NH_2 and CO_2 is infinitely fast i.e. the state of the chemical equilibrium is reached in every time step of the simulation. This allows summing up Eqs. (2) and (3) obtaining the expression for $c_{CO2} = [CO_2] + [P]$

$$\partial c_{CO2}/\partial t + \nabla \cdot \left(-\overline{D_{CO2P}}\nabla c_{CO2} - c_{CO2}\nabla\overline{D_{CO2P}}\right) = 0 \tag{5}$$

where $\overline{D_{CO2P}} = D_{CO2}h_{CO2} + D_Ph_P$ is the effective diffusion coefficient that depends on molar fractions $h_{CO2} = [CO_2]/c_{CO2}$ and $h_P = [P]/c_{CO2}$. These fractions may be expressed as a function of K and $[NH_2NH_2]$

$$\overline{D_{CO2P}} = D_{CO2}[1/(1 + K[NH_2NH_2])] + D_P[1 - 1/(1 + K[NH_2NH_2])] \tag{6}$$

In this way, the chemical equilibrium equation of the bulk reaction (Eq. (15)) is included in the continuity equation formulated for c_{CO2} (Eq. (5)). In the chemical equilibrium state reaction rate terms in Eq. (1) cancel each other leading to the set of homogeneous expressions

$$\partial[\text{NH}_2\text{NH}_2]/\partial t + \nabla.(-D_{\text{NH2NH2}}\nabla[\text{NH}_2\text{NH}_2]) = 0 \tag{7}$$

$$\partial\left[P'\right]/\partial t + \nabla.\left(-D_{P'}\nabla\left[P'\right]\right) = 0 \tag{8}$$

Altogether three continuity equations are formulated and solved for c_{CO2} (Eq. (5) including Eq. (15)), $[NH_2NH_2]$ (Eq. (7)) and $[P']$ (Eq. (8)).

3.4. Boundary conditions

For both kinetic and thermodynamic computational model the left boundary of the domain represents the electrode (Fig. 2, red line). Here, non-zero flux Neumann boundary condition is formulated for continuity equations governing $[NH_2NH_2]$ and $[P']$

$$-n \cdot (-D_{\text{NH2NH2}}\nabla[\text{NH}_2\text{NH}_2]) = -k_f^{el}[\text{NH}_2\text{NH}_2] + k_b^{el}\left[P'\right]$$
$$= -k^0[\text{NH}_2\text{NH}_2]\exp\left[(n-\alpha)F\left(E - E^0\right)/RT\right] \tag{9}$$

$$-n \cdot \left(-D_{P'}\nabla\left[P'\right]\right) = k_f^{el}[\text{NH}_2\text{NH}_2] - k_b^{el}\left[P'\right]$$
$$= k^0[\text{NH}_2\text{NH}_2]\exp\left[(n-\alpha)F\left(E - E^0\right)/RT\right] \tag{10}$$

A Butler-Volmer kinetic term was employed to express the rate constant k_f^{el} [67]. We set $k_b^{el} = 0$ as the NH_2NH_2 oxidation process is irreversible. On other three boundaries representing insulating walls (blue lines) a zero flux Neumann boundary condition was applied. As clearly demonstrated by cyclic voltammetric experiments (see Results and Discussion for details), CO_2 and P are both electrochemically inactive in the electrode potential region relevant to this work. Therefore, a zero flux Neumann boundary condition was set to all four boundaries in equations governing $[CO_2]$ and $[P]$.

The initial concentration value of the hydrazine oxidation product $[P']$ was uniformly set to zero in the whole domain. Initial values of $[NH_2NH_2]$, $[CO_2]$ and $[P]$ were uniformly set to values calculated respecting the equilibrium condition $K/c^0 = [P]/[NH_2NH_2][CO_2]$ (taking experimentally determined K value) and satisfying values of the total concentration of NH_2NH_2 and CO_2 (expressed as $[NH_2NH_2] + [P]$ and $[CO_2] + [P]$) reconstructing initially introduced amounts of reactants in experiments.

4. Results and discussion

4.1. Electrochemical measurements

Functional electrochemical devices require electrodes with high and well-defined area of the active surface and minimal kinetic hindrance for the charge transfer between the electrode and the electrolyte. In our recent publications [40–42] we demonstrated that properly activated electrodes manufactured from conductive composites by FDM 3DP may approach charge transfer characteristics typical for conventionally prepared metallic or carbon electrodes. We apply the printing-activation protocol developed for the PLA-CNT composite [41] to manufacture electrodes that are further integrated to the electrochemical platform devised in this work (see Experimental Section and Supplementary Information for details).

Charge transfer characteristics of such manufactured PLA-CNT electrodes were inspected by measuring cyclic voltammetry response in the aqueous electrolyte containing Ru(acac)$_3$ as the electroactive probe as discussed in the Experimental Section. A detailed description of data analysis has been reported previously [41]. The black curve in Fig. 3 shows a characteristic cyclic voltammogram of the activated PLA-CNT electrode prepared in this work. Both positive and negative potential scans show a well-developed Faradaic feature. The separation between the cathodic (-550 mV)
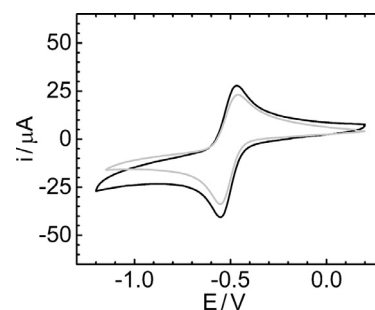
Fig. 3. Characteristic cyclic voltammogram of non-activated (grey) and activated (black) 3DP PLA-CNT electrode (geometrical area of 0.84 cm²) obtained in deaerated aqueous 0.1 M K$_2$SO$_4$ containing 5×10^{-4} M Ru(acac)$_3$ electroactive probe at 25 mV s^{-1}. Electrode potential values are stated against Ag/AgCl/3 M LiCl RE.

and anodic (-470 mV) peak is 80 mV indicating that the 3DP electrode causes almost no kinetic hindrance for the interfacial charge transfer. The comparison of the cathodic Faradaic peak current value with that calculated theoretically from the Randles-Sevcik equation for given conditions reveals that 91 % of the electrode/electrolyte interface is electrochemically active. Importantly, peak-to-peak separation and relative area of electrochemically active electrode surface are well comparable to those obtained previously in a conventional glass electrochemical cell (72 mV and 93 %) [41]. For comparison, the grey curve in Fig. 3 additionally depicts a cyclic voltammogram obtained for a non-activated PLA-CNT electrode. The peak-to-peak separation is 90 mV and the relative area of electrochemically active electrode surface amounts to 80 %. This indicates that the electrochemical activation improves both charge transfer characteristics of PLA-CNT electrodes.

The devised electrochemical platform was further employed to investigate the oxidation of aqueous NH_2NH_2 coupled to its chemical reaction with CO_2. At the interface of aqueous electrolytes and platinum electrodes, NH_2NH_2 undergoes an irreversible oxidation [68]

$$\text{NH}_2\text{NH}_2 \rightarrow \text{N}_2 + 4\text{H}^+ + 4\text{e}^- \tag{11}$$

In our work, costly and environmentally problematic platinum has been replaced by electrodes manufactured by FDM 3DP from the composite filament based on inexpensive and biodegradable PLA polymer. First, the ability of 3DP electrodes to detect and quantify NH_2NH_2 was explored in argon-saturated 0.1 M K$_2$SO$_4$ supporting electrolyte in the absence of CO_2. Grey curve in Fig. 4A shows a characteristic cyclic voltammogram obtained in the solution of 3.85×10^{-3} M NH_2NH_2. This concentration level is denoted further as $c_{0,\ NH2NH2}$ and serves as a reference for subsequent analysis of NH_2NH_2/CO_2 reaction mixtures (vide infra) by cyclic voltammetry. The potential scan starting at -0.50 V (all potential values are stated against Ag/AgCl/3 M LiCl RE) shows a pronounced anodic feature at 0.45 V attributed to the oxidation of NH_2NH_2. Results of measurements performed in solutions with varied NH_2NH_2 concentration c_{NH2NH2} indicate that the Faradaic anodic peak current i_{FA} is linearly proportional to c_{NH2NH2} (Fig. 4B) and for $c_{0,\ NH2NH2}$ it amounts to $i_{FA}^0 = (1.8 \pm 0.1) \times 10^{-4}$ A. The observed proportionality between the concentration and the resulting Faradaic response confirms the applicability of activated 3DP PLA-CNT electrodes for the quantification of NH_2NH_2 in the aqueous solution by cyclic voltammetry.

The response detected upon reversing the potential scan following the oxidation of NH_2NH_2 involves a small cathodic wave below -0.40 V. The same feature was observed also in the absence of hydrazine (grey curve in Fig. 4D). This control experiment additionally depicts a small anodic wave above +0.95 V. Results of experiments performed with varied WE potential limits (cyclic voltam-
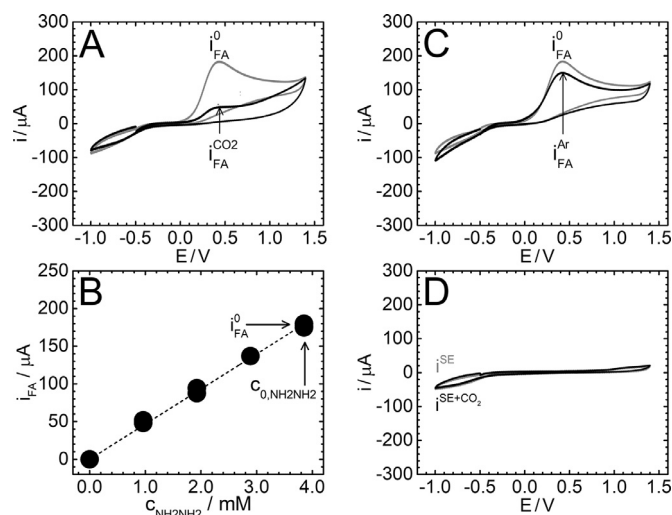
Fig. 4. Characteristic cyclic voltammogram of an activated 3DP PLA-CNT electrode in deaerated aqueous 0.1 M K_2SO_4 supporting electrolyte containing 3.85×10^{-3} M NH_2NH_2 prior to (grey) and upon (black) introducing 1.5 mL of saturated aqueous solution of (A) CO_2 and (C) Ar. (B) Faradaic anodic peak current i_{FA} as a function of hydrazine concentration c_{NH2NH2} (without gaseous solutions introduced). (D) Response obtained in the supporting electrolyte (SE) prior to (grey) and upon (black) introducing 1.5 mL of saturated aqueous CO_2 solution (in the absence of NH_2NH_2). All cyclic voltammograms were obtained at electrodes with geometrical area of 0.84 cm^2 at 25 mV s^{-1}. Electrode potential values are stated against Ag/AgCl/3 M LiCl RE.

mograms not shown) confirm that these two baseline features are related. The anodic feature is ascribed to the oxidation of redox-active, presumably oxygen groups on the surface of CNTs and the cathodic feature to their subsequent reduction. Importantly, the absence of cathodic features attributable to NH_2NH_2 indicates that its oxidation is followed by a fast decomposition of electrogenerated products. We assume that nitrogen is the final product of the hydrazine oxidation following the reaction pathway reported for platinum electrodes (Eq. (11)) [68].

Values of i_{FA} obtained at varied c_{NH2NH2} were further compared to theoretical predictions. For a chemically irreversible process (backward charge transfer reaction absent) realised in the voltammetric regime the theoretical Faradaic peak current is

$$i_F^{theor} = kn\alpha^{1/2}AcD^{1/2}\nu^{1/2} \qquad (12)$$

where $k = 2.99 \times 10^5$ A s mol^{-1} $V^{-1/2}$, α is the charge transfer coefficient, A is the active electrode/electrolyte interface area, c is the bulk concentration of electroactive species, D is its diffusion coefficient, n is the number of transferred electrons and ν is the electrode polarization rate [67]. For $c = c_{0,NH2NH2}$, values of ν and A as used in experiments (see Experimental Section) and assuming that $n = 4$ (Eq. (11)), $\alpha = 0.5$ and $D = 2.37 \times 10^{-5}$ cm^2 s^{-1} (determined for NH_2NH_2 in its aqueous solution in Ref. [65]) the i_F^{theor} value amounts to 2.1×10^{-3} A. Comparison of this value and the experimentally obtained i_{FA}^0 value gives the i_{FA}^0/i_F^{theor} ratio of 8.6 % i.e. far below unity. We note that such low value cannot be rationalized by a low electrochemical activity of the electrode surface as the i_{FC}^0/i_F^{theor} value of 91 % was found for the Ru(acac)$_3$ electroactive probe at the same electrode. To further explore this behaviour, we performed control measurements employing conventional glassy carbon (GC) electrodes (cyclic voltammograms not shown) and obtained the ratio of $i_{FA}^0/i_F^{theor} = 9.7$ %. We additionally inspected the data reported for the electrochemical oxidation of NH_2NH_2 on GC electrodes in Ref. [65] and obtained i_{FA}^0/i_F^{theor} value in the range of 10 – 20 %. Our analysis of the data reported for the NH_2NH_2 oxidation on platinum ultramicroelectrodes [68] leads to the i_{FA}^0/i_F^{theor} value of 40 %. In summary, i_{FA}^0/i_F^{theor} values obtained

for the NH_2NH_2 oxidation at different electrode surfaces are all well below unity and the observed anomaly is thus not specific to 3DP PLA-CNT electrodes. This observation suggests that a considerable portion of NH_2NH_2 molecules does not undergo the oxidation at the electrode/electrolyte interface, which is most likely caused by a deactivation or blocking of the electrode surface by reaction intermediates. Importantly for our current work, experimentally found linear proportionality between c_{NH2NH2} and i_{FA} at activated 3DP PLA-CNT electrodes (Fig. 4B) allows their employment for the quantification of NH_2NH_2 in its reaction mixtures with CO_2.

Subsequently, aqueous electrolyte containing dissolved CO_2 was investigated by cyclic voltammetry as follows. Varied volumes of water saturated by CO_2 (0.5 to 2.0 mL, see Experimental Section for details) were introduced to deaerated 0.1 M K_2SO_4 supporting electrolyte in the absence of NH_2NH_2. The black curve in Fig. 4D displays a characteristic cyclic voltammogram obtained in the electrolyte containing 3.28×10^{-3} M CO_2 (corresponding to the addition of 1.5 mL of its saturated aqueous solution). It is indistinguishable from that obtained in the absence of CO_2 shown in grey. Identical cyclic voltammograms were obtained upon introducing 0.5, 1.0 and 2.0 mL of the saturated CO_2 solution to the supporting electrolyte (results not shown). This indicates that CO_2 is electrochemically inactive in the inspected potential region and its introduction does not affect the accessible potential window of the supporting electrolyte. Importantly, this finding simplifies further analysis of cyclic voltammograms obtained in the reaction mixtures of NH_2NH_2 and CO_2 and allows the equilibrium NH_2NH_2 concentration $[NH_2NH_2]$ to be reliably determined.

The black curve in Fig. 4A displays a characteristic cyclic voltammogram obtained upon introducing 1.5 mL of water saturated by CO_2 to the NH_2NH_2 solution and homogenizing such obtained reaction mixture for 5 minutes. The Faradaic response of NH_2NH_2 obtained upon introducing CO_2 (i_{FA}^{CO2}) is lower compared to that before (i_{FA}^0) indicating that the reaction between the two species takes place. At this point we note that the baseline of the cyclic voltammetric response of the pure supporting electrolyte remained unchanged upon introducing CO_2 (Fig. 4D), which rules out the adsorption of CO_2 at the electrode/electrolyte interface. Therefore, observed changes of the hydrazine response cannot be caused by blockage of the electrode by adsorbed CO_2. Importantly, no new features appear suggesting that the reaction product (denoted as P further in the text) is electrochemically inactive in the inspected potential region and does not interfere with the response of NH_2NH_2. Most likely, the oxidation potential of P is beyond the electrode potential region inspected in this work.

According to Eq. (12) the Faradaic peak current is proportional to the bulk concentration of electroactive species and the area of electrochemically active electrode surface. The decrease of the NH_2NH_2 concentration is due to its consumption by the reaction with CO_2 as well as due to the dilution of reactants by their mixing. The active area may be reduced by the electrode deactivation caused by intermediates generated in the NH_2NH_2 oxidation process. Its contribution to the observed decrease of the Faradaic response was quantified by control experiments in which an argon gas was introduced to the system instead of CO_2.

Fig. 4C shows characteristic cyclic voltammograms obtained before (grey curve) and after (black curve) introducing 1.5 mL of water saturated by Ar to the solution of NH_2NH_2. Fig. 5A summarizes values of i_{FA}^{CO2}/i_{FA}^0 and i_{FA}^{Ar}/i_{FA}^0 as a function of introduced gas volume. Values of i_{FA}^{CO2}/i_{FA}^0 substantially decrease with added volume, reaching the value below 0.20 for 2.0 mL, while values of i_{FA}^{Ar}/i_{FA}^0 are significantly higher, being in the interval between 0.74 and 0.80 for all values of added volume. For Ar, observed changes account for the dilution of the NH_2NH_2 solution and the deactivation of the electrode surface. It is worth reminding that the electrode deactivation is specific to the NH_2NH_2 oxidation process as no decrease
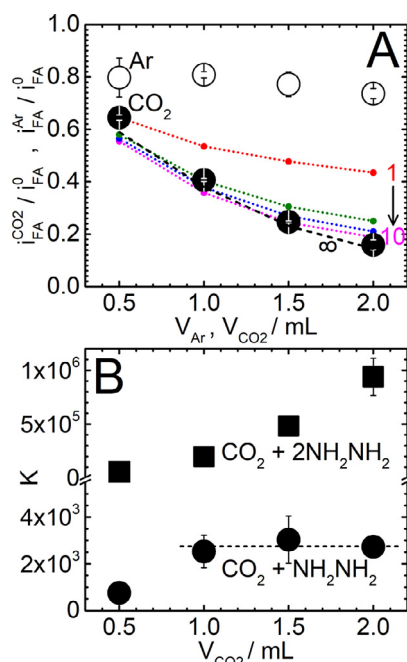
Fig. 5. (A) Experimentally determined i_{FA}^{CO2}/i_{FA}^0 (full circles) and i_{FA}^{Ar}/i_{FA}^0 (empty circles) values as a function of introduced gas volume. Shown data (average values and standard deviations) were obtained in two independent experimental campaigns. Theoretical values of i_{FA}^{CO2}/i_{FA}^0 obtained by finite-element-method numerical simulations assuming 1/1 reaction stoichiometry employing kinetic (coloured dotted lines) and thermodynamic (black dashed line, ∞) model. Numbers denote values of k_f^{bulk} (1, 5, 7 and 10) in 10^9 M^{-1} s^{-1} employed in the kinetic model. (B) Values of K obtained from experimentally obtained data shown in (A) for different V_{CO2} values assuming 1/1 (circles) and 1/2 (squares) reaction stoichiometry.

of the Faradaic response was registered upon repeated electrode potential cycling in the solution of $Ru(acac)_3$ (data not shown).

4.2. Analysis of experimentally obtained results

Assuming the volume additivity the dilution contribution $c_{Ar, NH2NH2}/c_{0, NH2NH2}$ may be expressed as $V_{NH2NH2}/(V_{NH2NH2} + V_{Ar})$. The electrode deactivation contribution is given by the ratio of electrochemically active surface area values after and before the introduction of Ar, A_{Ar}/A_0. Following Eq. (12), this ratio may be expressed as

$$A_{Ar}/A_0 = i_{FA}^{Ar}/i_{FA}^0 \times (V_{NH2NH2} + V_{Ar})/V_{NH2NH2} \qquad (13)$$

Values determined for all V_{Ar} values average to $\langle A_{Ar}/A_0 \rangle = 0.835 \pm 0.016$. The equilibrium NH_2NH_2 concentration $[NH_2NH_2]$ in reaction mixtures was determined from the ratio of Faradaic response obtained after and before introducing CO_2, i_{FA}^{CO2}/i_{FA}^0 taking the effect of the electrode deactivation into account

$$[NH_2NH_2] = c_{0,NH2NH2} \times i_{FA}^{CO2}/i_{FA}^0 \times \langle A_{Ar}/A_0 \rangle^{-1} \qquad (14)$$

The equilibrium amount of substance n_{NH2NH2} was determined as $[NH_2NH_2](V_{NH2NH2} + V_{CO2})$ and further employed to obtain equilibrium concentration values of CO_2, $[CO_2]$ and the reaction product P, $[P]$ as follows.

CO_2 dissolved in an aqueous environment forms a diprotic carbonic acid and NH_2NH_2 is a dibasic alkali. Therefore, the reaction between these two reactants may proceed following different stoichiometric ratios expressed by a generalized chemical reaction

$$\nu_{CO2}CO_2 + \nu_{NH2NH2}NH_2NH_2 \rightleftharpoons P \qquad (15)$$

Stoichiometric ratios ν_{CO2}/ν_{NH2NH2} of 1/1, 1/2 and 2/1 are considered as possible in this work. For the three scenarios the reac-

tion extent ξ was calculated from the NH_2NH_2 consumption

$$\xi = (c_{0,NH2NH2}V_{NH2NH2} - n_{NH2NH2})/\nu_{NH2NH2} \qquad (16)$$

Such obtained ξ values were employed to determine equilibrium concentration values of CO_2 and P

$$[CO_2] = (c_{0,CO2}V_{CO2} - \nu_{CO2}\xi)/(V_{NH2NH2} + V_{CO2}) \qquad (17)$$

$$[P] = \xi/(V_{NH2NH2} + V_{CO2}) \qquad (18)$$

where $c_{0, CO2}$ is the concentration of CO_2 in its saturated aqueous solution (see Experimental section for more details). Equilibrium concentration values (referenced to $c^0 = 1$ M) were utilized to obtain the equilibrium constant K as

$$K = [P](c^0)^{\nu_{CO2}+\nu_{NH2NH2}-1}/[CO_2]^{\nu_{CO2}}[NH_2NH_2]^{\nu_{NH2NH2}} \qquad (19)$$

The calculation performed for $\nu_{CO2}/\nu_{NH2NH2} = 2/1$ results in $[CO_2] < 0$ M ruling out this stoichiometric scenario. For $\nu_{CO2}/\nu_{NH2NH2} = 1/2$ one obtains $[CO_2] > 0$ M and resulting values of K range from 6.0×10^4 to 9.4×10^5 (Fig. 5B, squares). A pronounced dependence of K values on V_{CO2} expressed as the ratio of their extreme values (15.4) suggests that the reaction between CO_2 and NH_2NH_2 does not follow this stoichiometric scenario. For the 1/1 case obtained values of K range from 7.6×10^2 to 3.0×10^3 (Fig. 5B, circles) showing significantly less pronounced trend (the ratio of extreme values is 3.9). Therefore, out of all proposed three scenarios the 1/1 stoichiometry is the most realistic one. The K value obtained for $V_{gas} = 0.5$ mL is most likely influenced by high scattering of i_{FA}^{Ar}/i_{FA}^0 values (Fig. 5A) and was thus left out from further analysis. Values obtained for higher V_{gas} values average to $\langle K \rangle = (2.8 \pm 0.6) \times 10^3$ (dashed line in Fig. 5B). We emphasize that depicted values of i_{FA}^{Ar}/i_{FA}^0, i_{FA}^{CO2}/i_{FA}^0 and K were obtained as an average of data acquired in two independent experimental campaigns performed on different days corroborating the validity of presented findings.

Lee et al. [53] have recently investigated the composition of reaction products in mixtures of CO_2 and NH_2NH_2 prepared by introducing gaseous CO_2 to concentrated (32 to 64 wt.%) aqueous solutions of NH_2NH_2. The chemical composition of reaction products was probed by nuclear magnetic resonance spectroscopy complemented by theoretical calculations. The authors arrived at the conclusion that the reaction stoichiometry changes depending on the ratio of initial amounts of substance $\chi = n_{0,CO2}/n_{0,NH2NH2}$. For $0 < \chi < 0.30$ hydrazinium mono-carbonate corresponding to the $\nu_{CO2}/\nu_{NH2NH2} = 1/1$ stoichiometry was obtained as the main reaction product while for $0.30 < \chi < 0.64$ dihydrazinium hydrazinedicarbamate ($\nu_{CO2}/\nu_{NH2NH2} = 2/3$) was found as the major product. Motivated by these results we further calculated values of K from our own experimental data (which were obtained at χ values ranging from 0.3 to 1.2) considering the 2/3 stoichiometry. The values of K thus obtained range from 2.8×10^{10} to 4.5×10^{11} (individual values not plotted). Their ratio amounts to 16.6 and is much higher than that determined for the 1/1 stoichiometry (3.9). This indicates that in diluted solutions of NH_2NH_2 as employed in our work the reaction between CO_2 and NH_2NH_2 follows the 1/1 reaction stoichiometry (i.e. forming hydrazine mono-carbamate) even at χ values higher than 0.3. The formation of hydrazine mono-carbamate in the reaction between hydrazine and carbon dioxide was also observed by Pollet et al. [69] who used this adduct as a precursor to form polymer gels. The average of K values obtained for the 1/1 reaction stoichiometry $\langle K \rangle = (2.8 \pm 0.6) \times 10^3$ is thus considered as the equilibrium constant value of the chemical reaction between NH_2NH_2 and CO_2 determined in our work. This value is three orders of magnitude higher than that reported for the reaction between CO_2 and ammonia [70] and one order of magnitude higher than that between CO_2 and monoethanolamine [71].
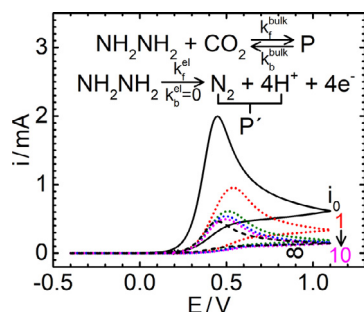
Fig. 6. Simulated response of the electrode/electrolyte interface in the system initially containing 3.85×10^{-3} M NH_2NH_2 in the entire computational domain (black solid curve). The response of the system with additionally introduced 3.28×10^{-3} M of CO_2 at $t = 0$ employing kinetic (coloured dotted curves) and thermodynamic (black dashed curve, ∞) model. Numbers denote values of k_f^{bulk} (1, 5, 7 and 10) in 10^9 M^{-1} s^{-1} employed in the kinetic model.

Because of that, we consider hydrazine as a suitable sorbent for the CO_2 capture.

4.3. Finite element method numerical simulations

The electrochemical oxidation of NH_2NH_2 coupled to its bulk chemical reaction with CO_2 was further modelled theoretically employing the finite element method numerical simulations in the environment of commercial software COMSOL Multiphysics®. [64] The developed computational model relies on formulating and solving a boundary value problem (a time-dependent continuity equation complemented by a set of boundary conditions) for concentration values of system constituents. Simulations were performed in a 2D rectangular computational domain (see Fig. 2 for details). The oxidation of NH_2NH_2 is described by non-zero flux Neumann boundary conditions at the boundary representing the electrode employing Butler-Volmer kinetic terms. Two individual computational approaches were developed and employed in this work, differing in the description of the chemical reaction between NH_2NH_2 and CO_2 in the electrolyte bulk. Both models consider 1/1 stoichiometry (reaction scheme is depicted in Fig. 6). The two approaches are further referred to as "kinetic" and "thermodynamic" model (for the formulation of respective boundary value problems see Calculation section).

In the kinetic model, four continuity equations are solved for individual system constituents – NH_2NH_2, CO_2, P and P; the latter cumulatively representing products of the hydrazine oxidation ($N_2 + 4H^+$). The bulk chemical equilibrium between NH_2NH_2 and CO_2 is taken into account by formulating reaction rate (source/sink) terms in respective continuity equations. The rate constant of the forward reaction k_f^{bulk} is estimated assuming that the reaction rate is limited by the diffusion of reactants

$$k_f^{bulk} = 8RT/3\eta \tag{20}$$

where $\eta = 9.6 \times 10^{-4}$ Pa s is the viscosity of the supporting electrolyte (aqueous 0.1 M K_2SO_4) [72]. At 298 K the k_f^{bulk} value amounts to 7×10^9 M^{-1} s^{-1}. As the Eqn 20) is an approximation we let the value of k_f^{bulk} to vary by ± 40 % i.e. to attain values between 5 and 10×10^9 M^{-1} s^{-1}. To account for slower reaction kinetics we further consider the value of 1×10^9 M^{-1} s^{-1}. Values of k_b^{bulk} were calculated from the relationship

$$K/c^0 = k_f^{bulk}/k_b^{bulk} \tag{21}$$

employing experimentally obtained equilibrium constant value $\langle K \rangle = 2.8 \times 10^3$ and k_f^{bulk} values determined by Eq. (20).

In the thermodynamic model the number of solved continuity equations is reduced to three by summing up relationships for-

mulated for CO_2 and P and evaluating the relative distribution of these two system constituents. The chemical equilibrium is taken into account by coupling such obtained distribution with the continuity equation expressed for NH_2NH_2, assuming the validity of the experimental $\langle K \rangle$ value. Reaction rate (source/sink) terms are completely omitted. The kinetic and the thermodynamic model are described in more detail in the Calculation Section.

In both models, initial values of concentration employed in simulations reconstruct the initial composition of experimentally prepared reaction mixtures (see Experimental Section for details). Both models were further complemented by time-dependent functions enabling the concentration profiles to be calculated at linearly varied values of the electrode potential $E(t)$. The value of the electric current i flowing through the electrode/electrolyte interface was obtained by integrating the current density

$$j = FnD_{NH2NH2}|\partial[NH_2NH_2]/\partial x|_{x=0} \tag{22}$$

over the boundary representing the electrode (see Fig. 2)

The solid black curve in Fig. 6 shows a simulated cyclic voltammogram of the system initially containing 3.85×10^{-3} M NH_2NH_2 in the entire computational domain i.e. in the absence of CO_2. Identical response was obtained by the kinetic and the thermodynamic approach. Importantly, the obtained Faradaic peak current value (2.0×10^{-3} A) is in a perfect agreement with the result of the closed-form solution (Eq. (12), 2.1×10^{-3} A). This verifies the correctness of computational models developed and employed in this work. The shape of the theoretical cyclic voltammogram corresponds to the experimentally obtained one (Fig. 4A and 4C, grey curve). Nonetheless, we note that the value of experimental (Fig. 4) and theoretical (Eq. (12) and Fig. 6) Faradaic peak current differs by one order of magnitude due to above-discussed low electroactivity of NH_2NH_2 molecules. Coloured dotted curves in Fig. 6 display the simulated cyclic voltammograms of the system with additionally introduced 3.28×10^{-3} M CO_2 at zero time, employing the kinetic model and k_f^{bulk} values varied as discussed above. This CO_2 concentration corresponds to the addition of 1.5 mL of its saturated aqueous solution in experiments. The effect of the electrode deactivation was taken into account by multiplying theoretically obtained $i(E)$ profiles by the experimentally determined value of $\langle A_{Ar}/A_0 \rangle$. Observed decrease of the Faradaic response reflects partial consumption of NH_2NH_2 due to its chemical reaction with CO_2. Theoretical values of i_{FA}^{CO2}/i_{FA}^0 obtained by the kinetic model at varied values of k_f^{bulk} and V_{CO2} are plotted as dotted curves in Fig. 5A. Results obtained for k_f^{bulk} ranging between 5 and 10×10^9 M^{-1} s^{-1} are in a very good agreement with experimentally obtained data-points (full black circles) while results calculated for 1×10^9 M^{-1} s^{-1} are clearly off the experimental trend. This confirms that the rate of the forward reaction is limited by the diffusion of reactants. Figs. 6 and 5A further depict results of simulations employing the thermodynamic model (black dashed curves). Such obtained dependence of i_{FA}^{CO2}/i_{FA}^0 on V_{CO2} is in a perfect agreement with experimental data and data obtained employing the kinetic model considering the highest value of k_f^{bulk}. The agreement between experimentally obtained and theoretically predicted data corroborates that the reaction between NH_2NH_2 and CO_2 has 1/1 stoichiometry and further indicates that its rate is limited by the diffusion of these two reactions partners.

4.4. Econometric analysis and applicability of the presented platform

Results obtained in this work demonstrate that the newly designed and manufactured integrated 3DP platform based on the PA12 cell and activated PLA-CNT composite electrodes is capable of a comprehensive electrochemical analysis of an interfacial charge transfer reaction (oxidation of NH_2NH_2) coupled to a

bulk chemical process (synthetic reaction between NH_2NH_2 and CO_2). Electrochemical experiments were complemented by finite-element-method numerical simulations employing two computational approaches utilizing the kinetic and the thermodynamic approach to formulate the bulk chemical reaction between NH_2NH_2 and CO_2. Obtained results indicate that the hydrazine oxidation is irreversible under given conditions, the bulk reaction between NH_2NH_2 and CO_2 has 1/1 reaction stoichiometry and the corresponding equilibrium constant amounts to $\langle K \rangle = (2.8 \pm 0.6) \times 10^3$.

The presented cyclic voltammetric analysis performed with activated 3DP PLA-CNT electrodes was additionally repeated with conventional platinum electrodes, providing very similar characteristics (results not shown). While platinum electrodes may be readily made by segmenting wires purchased from commercial sources, the manufacture of PLA-CNT electrodes requires the possession of the CAD software and the 3D printer. Currently, the unit price of the PLA-CNT composite is roughly 750 times lower than that of high purity platinum. The cell prototype devised and manufactured in this work consumed material (polyamide 12) worth of 1.8 Euro. This offers significant reduction of operational expenses in the electrode as well as cell manufacturing. Moreover, the combination of CAD modelling with bi-material 3D printing offers integrated electrochemical designs to be easily manufactured with multitude of sizes and shapes. Importantly, the presented cell design combines advanced functionalities that include separate WE, RE and CE compartments, inlet/outlet system to deoxygenate the electrolyte and an interface that enables air-tight introduction of reactants during the experiment. An outstanding performance of the platform was additionally verified by investigating characteristics of the electron transfer between activated 3DP PLA-CNT electrodes and aqueous electrolytes containing $Ru(acac)_3$ electroactive probe. Analysis of obtained data confirms that these electrodes have near-unity relative area of the electrochemically active surface and show almost no kinetic hindrance to the interfacial charge transfer. Electrochemical cells derived from the presented design are currently being applied to investigate electrochemical properties of biologically active compounds at polarized liquid-liquid interfaces [34,73,74]. In response to current healthcare crisis due to Covid 19, microchannels based on architectures developed in this work are being integrated within lab-on-a-chip microfluidic devices dedicated to the analysis of human viruses [75,76]. The presented design with integrated PLA-CNT electrodes will be further utilized as an electroanalytical platform to detect and quantify environmentally problematic nitrite [77] and nitrogen monoxide [78] in aqueous solutions. Additionally, an electrochemical reactor dedicated for the conversion of aqueous nitrite to ammonia as added-value chemical [79] is currently being developed. Computational models devised to simulate interfacial electron transfer processes and coupled bulk chemical reactions will be generalized by formulating electrodiffusion equations *i.e.* taking charge electroneutrality as well as ion migration in time-dependent electric fields into account [80,81].

5. Conclusions

In this work, we have devised and manufactured an integrated electrochemical platform employing computer assisted design combined with bi-material fused deposition modelling 3D printing. Polyamide PA12 filament was utilized to manufacture the electrochemical cell while polylactic acid-carbon nanotube composite was employed as the electrode material. The cell design involves separate compartments for reference and counter electrode connected to the central working electrode compartment by microholes. In-built gas inlet/outlet system enables the deoxygenation of the electrolyte and a specially designed interface allows reactants to be introduced to the cell in the course of the experiment. The

functionality of the manufactured platform was verified by the inspection of the electron transfer between anodically activated electrodes and $Ru(acac)_3$ electroactive probe dissolved in the aqueous electrolyte by cyclic voltammetry. Obtained characteristics confirm near-unity relative area of electrochemically active electrode surface and virtually no kinetic hindrance for the electron transfer.

The manufactured platform was further applied to investigate the electrochemical oxidation of aqueous hydrazine coupled to its bulk reaction with carbon dioxide. Cyclic voltammograms of hydrazine solutions obtained in the absence of carbon dioxide confirm that hydrazine undergoes a totally irreversible electrooxidation similarly to the reported works employing platinum electrodes. Concentration-resolved experiments confirmed a linear proportionality between the Faradaic response of hydrazine and its bulk concentration. This allowed cyclic voltammetry to be used as a tool to determine the concentration of unreacted hydrazine in its reaction mixtures with carbon dioxide. Results obtained at systematically varied concentration ratios allowed the value of the equilibrium constant to be determined employing reaction models considering diverse stoichiometric scenarios. The analysis of obtained results leads to the conclusion that under experimental conditions as used in this work the hydrazine reacts with carbon dioxide with the stoichiometric ratio of 1/1 and the corresponding K value amounts to $(2.8 \pm 0.6) \times 10^3$.

The finite element method numerical simulations were employed to reconstruct experimentally observed Faradaic currents of the hydrazine oxidation as a function of the amount of introduced carbon dioxide to the system. Two particular computational models were developed, differing in the definition of the homogeneous reaction between hydrazine and carbon dioxide (kinetic vs. thermodynamic model). The best agreement between computed Faradaic response and corresponding experimental data was obtained when the homogeneous reaction between carbon dioxide and hydrazine was considered as very fast i.e. limited by the diffusion of reactants. Therefore, the rate of the electrochemical hydrazine oxidation is limited by its diffusion towards the electrode as well as by kinetics of the electron transfer but not by the homogeneous reaction between hydrazine and carbon dioxide.

Importantly, our work is the first reported application of 3D printed electrodes and cells in the electrochemical analysis of an interfacial electron transfer process coupled to a bulk chemical reaction. We are convinced that the integrated 3D printed platform and computational approaches developed and presented in this work will find use in exploring systems in physical and environmental electrochemistry as well as in electroanalytical applications.

Declaration of Competing Interest

The authors declare no conflict of interests.

CRediT authorship contribution statement

João Giorgini Escobar: Conceptualization, Methodology, Validation, Formal analysis, Investigation. **Eva Vaněčková:** Conceptualization, Methodology, Validation, Formal analysis, Investigation. **Štěpánka Nováková Lachmanová:** Funding acquisition, Writing - review & editing. **Federico Vivaldi:** Conceptualization, Methodology, Writing - review & editing. **Jan Heyda:** Conceptualization, Methodology, Writing - review & editing. **Jiří Kubišta:** Conceptualization, Methodology, Writing - review & editing. **Violetta Shestivska:** Investigation, Writing - review & editing. **Patrik Španěl:** Conceptualization, Methodology, Writing - review & editing. **Karolina Schwarzová-Pecková:** Funding acquisition, Writing - review & editing. **Jiří Rathouský:** Funding acquisition, Writing - review & editing. **Táňa Sebechlebská:** Conceptualization, Methodology, Validation, Formal analysis, Investigation, Resources, Writing

Supplementary materials

Supplementary material associated with this article can be found, in the online version, at doi:10.1016/j.electacta.2020.136984.

References

[1] A. Arivarasi, A. Kumar, Classification of challenges in 3D printing for combined electrochemical and microfluidic applications: a review, Rapid Prototyping J. 25 (2019) 1328–1346.

[2] C.Y. Lee, A.C. Taylor, A. Nattestad, S. Beirne, G.G. Wallace, 3D printing for electrocatalytic applications, Joule 3 (2019) 1835–1849.

[3] M.D. Symes, P.J. Kitson, J. Yan, C.J. Richmond, G.J.T. Cooper, R.W. Bowman, T. Vilbrandt, L. Cronin, Integrated 3D-printed reactionware for chemical synthesis and analysis, Nat. Chem. 4 (2012) 349–354.

[4] M.P. Browne, E. Redondo, M. Pumera, 3D printing for electrochemical energy applications, Chem. Rev. 120 (2020) 2783–2810.

[5] C. Zhao, C.Y. Wang, R. Gorkin, S. Beirne, K.W. Shu, G.G. Wallace, Three dimensional (3D) printed electrodes for interdigitated supercapacitors, Electrochem. Commun. 41 (2014) 20–23.

[6] X.L. Huang, S. Chang, W. Siang, V. Lee, J. Ding, J.M. Xue, Three-dimensional printed cellular stainless steel as a high-activity catalytic electrode for oxygen evolution, J. Mater. Chem. A 5 (2017) 18176–18182.

[7] A. Ambrosi, M. Pumera, Multimaterial 3D-printed water electrolyzer with earth-abundant electrodeposited catalysts, ACS Sustain. Chem. Eng. 6 (2018) 16968–16975.

[8] A. Ambrosi, M. Pumera, Self-contained polymer/metal 3D printed electrochemical platform for tailored water splitting, Adv. Funct. Mater. 28 (2018) 1700655.

[9] G.Q. Yang, J.K. Mo, Z.Y. Kang, Y. Dohrmann, F.A. List, J.B. Green, S.S. Babu, F.Y. Zhang, Fully printed and integrated electrolyzer cells with additive manufacturing for high-efficiency water splitting, Applied Energy 215 (2018) 202–210.

[10] S.M.H. Hashemi, P. Karnakov, P. Hadikhani, E. Chinello, S. Litvinov, C. Moser, P. Koumoutsakos, D. Psaltis, A versatile and membrane-less electrochemical reactor for the electrolysis of water and brine, Energ. Environ. Sci. 12 (2019) 1592–1604.

[11] E. Achilli, A. Minguzzi, A. Visibile, C. Locatelli, A. Vertova, A. Naldoni, S. Rondinini, F. Auricchio, S. Marconi, M. Fracchia, P. Ghigna, 3D-printed photo-spectroelectrochemical devices for in situ and in operando X-ray absorption spectroscopy investigation, J. Synchrotron Radiat. 23 (2016) 622–628.

[12] M.F. Santangelo, I. Shtepliuk, D. Filippini, D. Puglisi, M. Vagin, R. Yakimova, J. Eriksson, Epitaxial graphene sensors combined with 3D-printed microfluidic chip for heavy metals detection, Sensors 19 (2019) 2393.

[13] G. Scordo, V. Bertana, L. Scaltrito, S. Ferrero, M. Cocuzza, S.L. Marasso, S. Romano, R. Sesana, F. Catania, C.F. Pirri, A novel highly electrically conductive composite resin for stereolithography, Mater. Today Commun. 19 (2019) 12–17.

[14] G.D. O'Neil, S. Ahmed, K. Halloran, J.N. Janus, A. Rodriguez, I.M.T. Rodriguez, Single-step fabrication of electrochemical flow cells utilizing multi-material 3D printing, Electrochem. Commun. 99 (2019) 56–60.

[15] E. Mousset, V.H. Weiqi, B.F.Y. Kai, J.S. Koh, J.W. Tng, Z.X. Wang, O. Lefebvre, A new 3D-printed photoelectrocatalytic reactor combining the benefits of a transparent electrode and the Fenton reaction for advanced wastewater treatment, J. Mater. Chem. A 5 (2017) 24951–24964.

[16] I. Lozano, C. Lopez, N. Menendez, N. Casillas, P. Herrasti, Design, construction and evaluation of a 3D printed electrochemical flow cell for the synthesis of magnetite nanoparticles, J. Electrochem. Soc. 165 (2018) H688–H697.

[17] V. Katseli, N. Thomaidis, A. Economou, C. Kokkinos, Miniature 3D-printed integrated electrochemical cell for trace voltammetric Hg(II) determination, Sensor. Actuator. B-Chem. 308 (2020) 127715.

[18] V. Katseli, A. Economou, C. Kokkinos, Single-step fabrication of an integrated 3D-printed device for electrochemical sensing applications, Electrochem. Commun. 103 (2019) 100–103.

[19] K.E. Guima, L.M. Alencar, G.C. da Silva, M.A.G. Trindade, C.A. Martins, 3D-printed electrolyzer for the conversion of glycerol into tartronate on Pd nanocubes, ACS Sustain. Chem. Eng. 6 (2018) 1202–1207.

[20] G.W. Bishop, J.E. Satterwhite, S. Bhakta, K. Kadimisetty, K.M. Gillette, E. Chen, J.F. Rusling, 3D-printed fluidic devices for nanoparticle preparation and flow-injection amperometry using integrated prussian blue nanoparticle-modified electrodes, Anal. Chem. 87 (2015) 5437–5443.

[21] R.M. Cardoso, D.M. Mendonça, W.P. Silva, M.N. Silva, E. Nossol, R.A. da Silva, E.M. Richter, R.A. Muñoz, 3D printing for electroanalysis: from multiuse electrochemical cells to sensors, Anal. Chim. Acta 1033 (2018) 49–57.

[22] C.P. de Leon, W. Hussey, F. Frazao, D. Jones, E. Ruggeri, S. Tzortzatos, R.D. McKerracher, R.G.A. Wills, S. Yang, F.C. Walsh, The 3D printing of a polymeric electrochemical cell body and its characterisation, Chem. Engineer. Trans. 41 (2014) 1–6.

[23] A.A. Dias, T.M.G. Cardoso, R.M. Cardoso, L.C. Duarte, R.A.A. Munoz, E.M. Richter, W.K.T. Coltro, Paper-based enzymatic reactors for batch injection analysis of glucose on 3D printed cell coupled with amperometric detection, Sensor. Actuator. B-Chem. 226 (2016) 196–203.

[24] M.F. dos Santos, V. Katic, P.L. dos Santos, B.M. Pires, A.L.B. Formiga, J.A. Bonacin, 3D-printed low-cost spectroelectrochemical cell for in situ Raman measurements, Anal. Chem. 91 (2019) 10386–10389.

[25] H.A. Figueredo-Rodriguez, R.D. McKerracher, C.P. de Leon, F.C. Walsh, Current distribution in a rectangular flow channel manufactured by 3-D printing, AIChE J. 63 (2017) 1144–1151.

[26] P. Rewatkar, M. Bandapati, S. Goel, Miniaturized additively manufactured co-laminar microfluidic glucose biofuel cell with optimized grade pencil bioelectrodes, Int. J. Hydrogen Energy 44 (2019) 31434–31444.

[27] E.M. Richter, D.P. Rocha, R.M. Cardoso, E.M. Keefe, C.W. Foster, R.A.A. Munoz, C.E. Banks, Complete additively manufactured (3D-printed) electrochemical sensing platform, Anal. Chem. 91 (2019) 12844–12851.

[28] D.M. Wirth, M.J. Sheaff, J.V. Waldman, M.P. Symcox, H.D. Whitehead, J.D. Sharp, J.R. Doerfler, A.A. Lamar, G. LeBlanc, Electrolysis activation of fused-filament–fabrication 3D-printed electrodes for electrochemical and spectroelectrochemical analysis, Anal. Chem. 91 (2019) 5553–5557.

[29] C.H. Yang, C.W. Chen, Y.K. Lin, Y.C. Yeh, C.C. Hsu, Y.J. Fan, I.S. Yu, J.Z. Chen, Atmospheric-pressure plasma jet processed carbon-based electrochemical sensor integrated with a 3D-printed microfluidic channel, J. Electrochem. Soc. 164 (2017) B534–B541.

[30] G. Chisholm, P.J. Kitson, N.D. Kirkaldy, L.G. Bloor, L. Cronin, 3D printed flow plates for the electrolysis of water: an economic and adaptable approach to device manufacture, Energ. Environ. Sci. 7 (2014) 3026–3032.

[31] S.E. Lowe, G. Shi, Y.B. Zhang, J.D. Qin, S.J. Wang, A. Uijtendaal, J.Q. Sun, L.X. Jiang, S.Y. Jiang, D.C. Qi, M. Al-Mamun, P.R. Liu, Y.L. Zhong, H.J. Zhao, Scalable production of graphene oxide using a 3D-printed packed-bed electrochemical reactor with a boron-doped diamond electrode, ACS Appl. Nano Mater. 2 (2019) 867–878.

[32] C.G.W. van Melis, M.R. Penny, A.D. Garcia, A. Petti, A.P. Dobbs, S.T. Hilton, K. Lam, Supporting-electrolyte-free electrochemical methoxymethylation of alcohols using a 3D-printed electrosynthesis continuous flow cell system, Chemelectrochem 6 (2019) 4144–4148.

[33] S. Damiati, S. Kupcu, M. Peacock, C. Eilenberger, M. Zamzami, I. Qadri, H. Choudhry, U.B. Sleytr, B. Schuster, Acoustic and hybrid 3D-printed electrochemical biosensors for the real-time immunodetection of liver cancer cells (HepG2), Biosens. Bioelectron. 94 (2017) 500–506.

[34] L. Poltorak, K. Rudnicki, V. Kolivoška, T. Sebechlebská, P. Krzyczmonik, S. Skrzypek, Electrochemical study of ephedrine at the polarized liquid-liquid interface supported with a 3D printed cell, J. Hazard. Mater. 402 (2021) 123411.

[35] Z. Rymansaib, P. Iravani, E. Emslie, M. Medvidovic-Kosanovic, M. Sak-Bosnar, R. Verdejo, F. Marken, All-polystyrene 3D-printed electrochemical device with embedded carbon nanofiber-graphite-polystyrene composite conductor, Electroanalysis 28 (2016) 1517–1523.

[36] C.W. Foster, M.P. Down, Y. Zhang, X.B. Ji, S.J. Rowley-Neale, G.C. Smith, P.J. Kelly, C.E. Banks, 3D printed graphene based energy storage devices, Sci. Rep. 7 (2017) 42233.

[37] N. Rohaizad, C.C. Mayorga-Martinez, F. Novotny, R.D. Webster, M. Pumera, 3D-printed Ag/AgCl pseudo-reference electrodes, Electrochem. Commun. 103 (2019) 104–108.

[38] J.R. Hudkins, D.G. Wheeler, B. Pena, C.P. Berlinguette, Rapid prototyping of electrolyzer flow field plates, Energ. Environ. Sci. 9 (2016) 3417–3423.

[39] T. Sebechlebska, E. Vaněčková, V. Shestivska, V. Kolivoška, in: Proceedings of the International Conference Modern Electrochemical Methods Xxxix, 2019, pp. 183–187.

[40] E. Vaneckova, M. Bousa, S.N. Lachmanova, J. Rathousky, M. Gal, T. Sebechlebska, V. Kolivoska, 3D printed polylactic acid/carbon black electrodes with nearly ideal electrochemical behaviour, J. Electroanal. Chem. 857 (2020) 113745.

[41] E. Vaneckova, M. Bousa, F. Vivaldi, M. Gal, J. Rathousky, V. Kolivoska, T. Sebechlebska, UV/VIS spectroelectrochemistry with 3D printed electrodes, J. Electroanal. Chem. 857 (2020) 113760.

[42] E. Vaneckova, M. Bousa, R. Sokolova, P. Moreno-Garcia, P. Broekmann, V. Shestivska, J. Rathousky, M. Gal, T. Sebechlebska, V. Kolivoska, Copper electroplating of 3D printed composite electrodes, J. Electroanal. Chem. 858 (2020) 113763.

[43] J.P. Hughes, P.L. dos Santos, M.P. Down, C.W. Foster, J.A. Bonacin, E.M. Keefe, S.J. Rowley-Neale, C.E. Banks, Single step additive manufacturing (3D printing) of electrocatalytic anodes and cathodes for efficient water splitting, Sustain. Energy Fuels. 4 (2020) 302–311.

[44] C.W. Foster, H.M. Elbardisy, M.P. Down, E.M. Keefe, G.C. Smith, C.E. Banks, Additively manufactured graphitic electrochemical sensing platforms, Chem. Eng. J. 381 (2020) 112343.

[45] V. Katseli, A. Economou, C. Kokkinos, A novel all-3D-printed cell-on-a-chip device as a useful electroanalytical tool: Application to the simultaneous voltammetric determination of caffeine and paracetamol, Talanta 208 (2020) 120388.

[46] C. Field, V. Barros, D. Dokken, K. Mach, M. Mastrandrea, P. Mastrandrea, L. White, Intergovernmental panel on climate change, Climate change 2014: Impacts, adaptation, and vulnerability, Contribution of Working Group II to the Fifth Assessment Report of the Intergovernmental Panel on Climate Change, Cambridge University Press Cambridge, New York, 2014.

[47] A.V. Rudnev, U.E. Zhumaev, A. Kuzume, S. Vesztergom, J. Furrer, P. Broekmann, T. Wandlowski, The promoting effect of water on the electroreduction of CO_2 in acetonitrile, Electrochim. Acta 189 (2016) 38–44.

[48] D. Vasilyev, E. Shirzadi, A.V. Rudnev, P. Broekmann, P.J. Dyson, Pyrazolium ionic liquid co-catalysts for the electroreduction of CO_2, ACS Appl. Energy Mater. 1 (2018) 5124–5128.

[49] S. Bishnoi, G.T. Rochelle, Absorption of carbon dioxide in aqueous piperazine/methyldiethanolamine, AIChE J. 48 (2002) 2788–2799.

[50] L. Faramarzi, G.M. Kontogeorgis, K. Thomsen, E.H. Stenby, Extended UNIQUAC model for thermodynamic modeling of CO_2 absorption in aqueous alkanolamine solutions, Fluid Phase Equilib. 282 (2009) 121–132.

[51] J.E. Rainbolt, P.K. Koech, C.R. Yonker, F. Zheng, J. Linehan, D.J. Heldebrant, Pressure-induced chemical and physical CO_2 capture with pure alkanolamines with pressure-swing regeneration, Abstracts Pap. Am. Chem. Soc. 241 (2011).

[52] N. Rodríguez, S. Mussati, N. Scenna, Optimization of post-combustion CO_2 process using DEA–MDEA mixtures, Chem. Eng. Res. Des. 89 (2011) 1763–1773.

[53] B. Lee, H.M. Stowe, K.H. Lee, N.H. Hur, S.J. Hwang, E. Paek, G.S. Hwang, Understanding CO_2 capture mechanisms in aqueous hydrazine via combined NMR and first-principles studies, Phys. Chem. Chem. Phys. 19 (2017) 24067–24075.

[54] K.H. Lee, B. Lee, J.H. Lee, J.K. You, K.T. Park, I.H. Baek, N.H. Hur, Aqueous hydrazine as a promising candidate for capturing carbon dioxide, Int. J. Greenh. Gas Con. 29 (2014) 256–262.

[55] J.-P. Schirmann, P. Bourdauducq, Hydrazine. Ullmann's Encyclopedia of Industrial Chemistry, Wiley-VCH, Weinheim, 2002 DOI, 10 a13_177.

[56] J.P. Chen, L.L. Lim, Key factors in chemical reduction by hydrazine for recovery of precious metals, Chemosphere 49 (2002) 363–370.

[57] A.K. Mosai, L. Chimuka, E.M. Cukrowska, I.A. Kotze, H. Tutu, The recovery of platinum (IV) from aqueous solutions by hydrazine-functionalised zeolite, Miner. Eng. 131 (2019) 304–312.

[58] L. Hong, L.J. Yin, D.Z. Chen, D. Wang, Proposal and verification of a kinetic mechanism model for NO_x removal with hydrazine hydrate, AIChE J. 61 (2015) 904–912.

[59] J.B. Lee, S.D. Kim, NOx reduction by hydrazine in a pilot-scale reactor, Chem. Eng. J. 69 (1998) 99–104.

[60] F. Wang, J.B. Gerken, D.M. Bates, Y.J. Kim, S.S. Stahl, Electrochemical strategy for hydrazine synthesis: development and overpotential analysis of methods for oxidative N-N coupling of an ammonia surrogate, J. Am. Chem. Soc. 142 (2020) 12349–12356.

[61] T. Sebechlebska, J. Sebera, V. Kolivoska, M. Lindner, J. Gasior, G. Meszaros, M. Valasek, M. Mayor, M. Hromadova, Investigation of the geometrical arrangement and single molecule charge transport in self-assembled monolayers of molecular towers based on tetraphenylmethane tripod, Electrochim. Acta 258 (2017) 1191–1200.

[62] J. Sebera, T. Sebechlebska, S. Novakova Lachmanova, J. Gasior, P.M. Garcia, G. Meszaros, M. Valasek, V. Kolivoska, M. Hromadova, Investigation of the charge transport in model single molecule junctions based on expanded bipyridinium molecular conductors, Electrochim. Acta 301 (2019) 267–273.

[63] O.S. Wolfbeis, B. Kovacs, K. Goswami, S.M. Klainer, Fiber-optic fluorescence carbon dioxide sensor for environmental monitoring, Microchimica Acta 129 (1998) 181–188.

[64] COMSOL Multiphysics® v. 5.4. www.comsol.com. COMSOL AB, Stockholm, Sweden. [accesed 10 Aug 2020].

[65] M.M. Ardakani, M.A. Karimi, M.M. Zare, S.M. Mirdehghan, Investigation of electrochemical behavior of hydrazine with alizarin as a mediator on glassy carbon electrode, Int. J. Electrochem. Sci. 3 (2008) 246–258.

[66] M.J.W. Frank, J.A.M. Kuipers, W.P.M. vanSwaaij, Diffusion coefficients and viscosities of CO_2+H_2O, CO_2+CH_3OH, NH_3+H_2O, and NH_3+CH_3OH liquid mixtures, J. Chem. Eng. Data 41 (1996) 297–302.

[67] A.J. Bard, L.R. Faulkner, Electrochemical Methods, Electrochemical Methods: Fundamentals and Applications, 2nd edition, Viley-VCH, USA, 2000.

[68] L. Aldous, R.G. Compton, The mechanism of hydrazine electro-oxidation revealed by platinum microelectrodes: role of residual oxides, Phys. Chem. Chem. Phys. 13 (2011) 5279–5287.

[69] P. Pollet, S. Samanta, R.P. Apkarian, L. Gelbaum, J. Leisen, C.L. Kitchens, K. Griffith, K. Richman, C.A. Eckert, C.L. Liotta, CO_2 promoted gel formation of hydrazine, monomethylhydrazine, and ethylenediamine: structures and properties, Ind. Eng. Chem. Res. 58 (2019) 22652–22662.

[70] X.G. Wang, W. Conway, D. Fernandes, G. Lawrance, R. Burns, G. Puxty, M. Maeder, Kinetics of the reversible reaction of CO_2(aq) with ammonia in aqueous solution, J. Phys. Chem. A 115 (2011) 6405–6412.

[71] N. McCann, D. Phan, X.G. Wang, W. Conway, R. Burns, M. Attalla, G. Puxty, M. Maeder, Kinetics and mechanism of carbamate formation from CO_2(aq), carbonate species, and monoethanolamine in aqueous solution, J. Phys. Chem. A 113 (2009) 5022–5029.

[72] I.M. Abdulagatov, N.D. Azizov, Thermal conductivity and viscosity of aqueous K_2SO_4 solutions at temperatures from 298 to 575K and at pressures up to 30 MPa, Int. J. Thermophys. 26 (2005) 593–635.

[73] K. Rudnicki, L. Poltorak, S. Skrzypek, E.J.R. Sudholter, FusedSilica microcapillaries used for a simple miniaturization of the electrified liquid-liquid interface, Anal. Chem. 90 (2018) 7112–7116.

[74] K. Rudnicki, L. Poltorak, S. Skrzypek, E.J.R. Sudholter, Ion transfer voltammetry for analytical screening of fluoroquinolone antibiotics at the water-1.2-dichloroethane interface, Anal. Chim. Acta 1085 (2019) 75–84.

[75] V. Kolivoska, V.U. Weiss, L. Kremser, B. Gas, D. Blaas, E. Kenndler, Electrophoresis on a microfluidic chip for analysis of fluorescence-labeled human rhinovirus, Electrophoresis 28 (2007) 4734–4740.

[76] V.U. Weiss, V. Kolivoska, L. Kremser, B. Gas, D. Blaas, E. Kenndler, Virus analysis by electrophoresis on a microfluidic chip, J. Chromatrogr. B. 860 (2007) 173–179.

[77] R.M. Cardoso, P.R.L. Silva, A.P. Lima, D.P. Rocha, T.C. Oliveira, T.M. do Prado, E.L. Fava, O. Fatibello-Filho, E.M. Richter, R.A.A. Munoz, 3D-Printed graphene/polylactic acid electrode for bioanalysis: Biosensing of glucose and simultaneous determination of uric acid and nitrite in biological fluids, Sensor. Actuator. B-Chem. 307 (2020) 127621.

[78] J.L. Erkal, A. Selimovic, B.C. Gross, S.Y. Lockwood, E.L. Walton, S. McNamara, R.S. Martin, D.M. Spence, 3D printed microfluidic devices with integrated versatile and reusable electrodes, Lab on a Chip 14 (2014) 2023–2032.

[79] A. Sahin, W.T. Lin, W.O. Khunjar, K. Chandran, S. Banta, A.C. West, Electrochemical reduction of nitrite to ammonia for use in a bioreactor, J. Electrochem. Soc. 160 (2013) G19–G26.

[80] T. Sebechlebska, P. Neogrady, I. Valent, A three-ions model of electrodiffusion kinetics in a nanochannel, Chem. Phys. Lett. 663 (2016) 33–39.

[81] I. Valent, P. Petrovic, P. Neogrady, I. Schreiber, M. Marek, Electrodiffusion kinetics of ionic transport in a simple membrane channel, J. Phys. Chem. B 117 (2013) 14283–14293.